remote sensing

Communication

The Different Characteristics of the Mass Transport between the Stratosphere and the Troposphere in Two Types of Cyclonic Rossby Wave-Breaking Events

Huiping Wang [1,2], Chunhua Shi [1,*] and Dong Guo [1]

[1] Key Laboratory of Meteorological Disaster, Ministry of Education (KLME), Joint International Research Laboratory of Climate and Environment Change (ILCEC), Collaborative Innovation Center on Forecast and Evaluation of Meteorological Disasters (CIC-FEMD), Nanjing University of Information Science and Technology, Nanjing 210044, China

[2] Qinghai Institute of Meteorological Sciences, Xining 810001, China

* Correspondence: shi@nuist.edu.cn

Abstract: Using the ERA5 reanalysis data and trajectory analysis provided by Hysplit4, a comparative analysis was conducted on the primary pathways of air particles and the dominant weather systems in two distinct cases of equatorward and poleward cyclonic Rossby wave-breaking (CWB) events. Subsequently, the characteristics of mass exchange between the stratosphere and troposphere in both CWBs were estimated and discussed. CWB events are frequently associated with the development of an upper front in subtropics and a ridge or blocking in mid-latitudes, leading to a tropopause anomaly characterized by a downward depression in the subtropics and an upward bulge in the mid-latitudes. High potential vorticity (PV) particles exhibit negligible vertical motion and are instead controlled by the circulation of the ridge or blocking, leading to a significant poleward transport. In contrast, low PV particles display noticeable vertical motion, with approximately one fourth of them ascending on the north side of the upper-level jet exit region. After CWB occurrence, approximately 25% of low PV particles moved southward and sank below 500 hPa with the downstream trough's cold air. Most high PV particles remained in the stratosphere, and low PV particles predominantly remained in the troposphere. Only a small proportion (2% to 6%) of particles underwent stratosphere–troposphere exchange (STE). In equatorward CWB, STE manifested as transport from stratosphere to troposphere, occurring mainly in 24–48 h post breaking with a maximum mass transport of approximately 1.54×10^{13} kg. In poleward CWB, STE involved transport from troposphere to stratosphere, occurring mainly within 0–18 h post breaking with a maximum mass transport of approximately 1.48×10^{13} kg.

Keywords: cyclonic Rossby wave-breaking; stratosphere–troposphere exchange; trajectory analysis

check for updates

Citation: Wang, H.; Shi, C.; Guo, D. The Different Characteristics of the Mass Transport between the Stratosphere and the Troposphere in Two Types of Cyclonic Rossby Wave-Breaking Events. *Remote Sens.* **2023**, *15*, 3286. https://doi.org/10.3390/rs15133286

Academic Editors: Wuke Wang, Yang Gao, Jiali Luo and Manuel Antón

Received: 25 May 2023
Revised: 20 June 2023
Accepted: 22 June 2023
Published: 26 June 2023

Copyright: © 2023 by the authors. Licensee MDPI, Basel, Switzerland. This article is an open access article distributed under the terms and conditions of the Creative Commons Attribution (CC BY) license (https://creativecommons.org/licenses/by/4.0/).

1. Introduction

Rossby wave breaking (RWB) is an atmospheric phenomenon characterized by the turning of the meridional gradient of potential vorticity (PV) from positive to negative on the isentropic surface near the extratropical high-level westerly jet chasm [1–3]. Two types of RWB have been identified, namely anticyclonic wave breaking (AWB) and cyclonic wave breaking (CWB), which are associated with different zonal wind shear [4]. RWB typically occurs near the dynamic tropopause, as determined by the PV gradient [5]. In the Northern Hemisphere, the occurrence of RWB is associated with the presence of a low (high) PV tongue extending eastwards and polewards (westwards and equatorwards) in the CWB, and a low (high) PV tongue extending westwards and polewards (eastwards and equatorwards) in the AWB [6–8].

RWB events are associated with severe distortion of the PV contours, as high PV contours stretch from the polar vortex system to low latitudes and low PV contours escape from the tropical tropopause layer to high latitudes, resulting in stratosphere–troposphere exchange (STE) [2,6,9–15]. This process involves the crossing of air masses across the tropopause, leading to the coupling of the troposphere and stratosphere, which have different dynamic, thermal, and chemical characteristics. STE can affect the radiation balance in the upper troposphere–lower stratosphere (UTLS) region, through the variation of water vapor and ozone near the tropopause [14,16–22]. Based on the direction of mass transport, STE can be divided into two types, namely troposphere-to-stratosphere transport (TST) and stratosphere-to-troposphere transport (STT). The RWB on the 380 K isentropic surface is often associated with the breakup of the subtropical westerly jet, which acts as a barrier for meridional transport. Baroclinic instability and wave breaking tend to lead to meridional transport and isentropic surface mixing in the most variable zone of the westerly jet [23–25].

The STE process operates at multiple scales, which are characterized by various physical processes, including meridional circulation, frontal transport, deep convective transport, and the thermal and dynamic effects of the South Asia high. These processes achieve STE through vertical circulation. However, the STE induced by RWB is unique in that there is no significant vertical motion, and the air mass is transported quasi-horizontally along the isentropic surface. Notably, the frequency of CWB is considerably lower than that of AWB, and research on its role in STE is limited. Therefore, this study examines two typical CWB cases and focuses on the characteristics and differences in TST and STT mass transport in the stratosphere and troposphere.

2. Data and Methods

2.1. Data

Meteorological data, ERA5, was sourced from the European Centre for Medium-Range Weather Forecasts (ECMWF) (https://cds.climate.copernicus.eu/cdsapp#!/search?type=dataset&text=ERA5, accessed on 7 March 2023). The daily reanalysis data set was utilized for analyzing the circulation field, specifically for the variables of potential height, zonal wind, meridional wind, vertical velocity, temperature, and potential vorticity. For trajectory analysis, hourly reanalysis data were used.

2.2. Methods

2.2.1. Trajectory Analysis Methods

The Hysplit4 trajectory model, a Eulerian–Lagrangian hybrid model, was employed to analyze the trajectory, diffusion, and sedimentation of air particles [26]. The model has been widely used in numerous studies, including those involving spatial diffusion of pollutants [27–31], water vapor transport [32–34], and STE [35,36].

The high PV particles (PV > 5.5 PVU) within polygon 1-2-3 and low PV particles (PV < 5.5 PVU) within polygon 2-3-4 in a RWB region were tracked separately in the Hysplit4 model (as shown in Figure 1). Tracer particles were placed at 0.25° intervals in both zonal and meridional directions, and tracked backward and forward for 48 h, respectively.

To cluster the trajectories from Hysplit4, the MeteoInfo application was used, which has a powerful capability in regional multi-trajectory clustering analysis [37]. Two trajectory clustering methods are available in MeteoInfo: Euclidean distance clustering and angular distance clustering [38]. In this study, Euclidean distance clustering was utilized, and the optimal number of clusters was determined by the maximum variation of total spatial variance in response to the number of clusters.

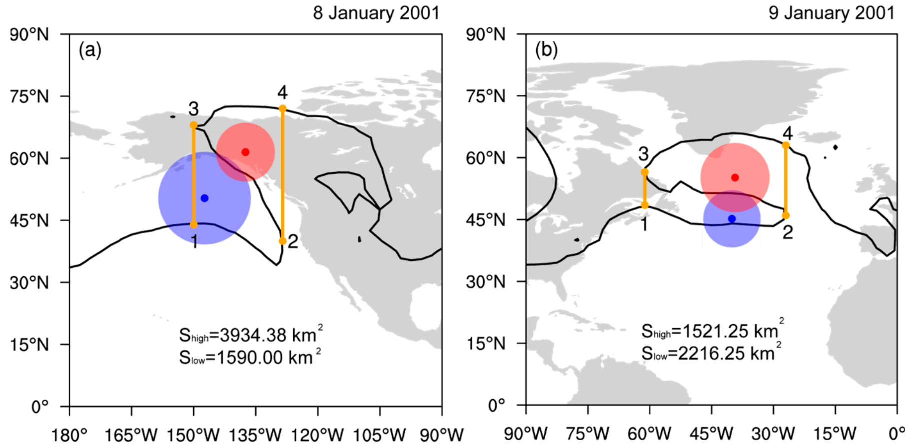

Figure 1. Schematic diagrams of equatorward CWB (**a**) and poleward CWB (**b**) on 330 K isentropic surface. The black curve is 5.5 PVU contour (1 PVU = 10^{-6} $m^2 \cdot s^{-1} \cdot K \cdot kg^{-1}$). The orange points 1, 2, 3, and 4 represent the intersections of the PV curve with the westernmost and easternmost meridians, where the PV curve intersects with each meridian multiple times. The red and blue circles represent the equivalent circle area of low PV in polygon 1-2-3 and high PV in polygon 2-3-4, respectively. The centers of circles represent the centroid positions for the polygons.

2.2.2. Quantitative Estimation of STE

Quantitative estimation of STE was conducted by calculating the PV values for each tracked particle along both forward and backward trajectories. A PV threshold of 6 PVU was used to classify particles in the stratosphere, while those with PV values below 4 PVU were considered to be in the troposphere. Particles with PV values ranging from 4 PVU to 6 PVU were classified as being in the transition layer [11,39–43]. Therefore, the percentages of stratospheric and tropospheric particles within the total particle population at each time step can be estimated.

The previous study demonstrated the presence of CWBs on the 330 K isentropic surface, with a distinct transition layer located at an altitude of approximately 10 km. Consequently, the initial altitude centers for the particles were designated as 9.8 km, 10.0 km, and 10.2 km, respectively. Each particle was allocated an initial horizontal extent of 0.25° × 0.25° and a vertical thickness (Z) of 0.2 km. The occupied volume (V) of a particle can be expressed in Equations (1)–(3):

$$V = XYZ \tag{1}$$

$$X = \frac{n\pi R cos\theta}{180^\circ} \tag{2}$$

$$Y = \frac{n\pi R}{180^\circ} \tag{3}$$

where X represents the zonal distance, Y represents the meridional distance, Z represents the vertical thickness, n is the horizontal resolution, R is the equatorial Earth radius (6.37×10^3 km), and θ represents the latitude.

The atmospheric density in this region can be estimated using Equation (4):

$$\rho_d = P \cdot {R_d}^{-1} \cdot T^{-1} \tag{4}$$

where R_d is 287 $J \cdot kg^{-1} \cdot K^{-1}$, P is pressure, and T is temperature. The mass of an individual particle can be obtained by multiplying its density by the volume it occupies.

3. Results

At mid-latitudes, the thermodynamic tropopause and the dynamic tropopause are generally consistent and located around the 330 K isentropic surface. The transition layer thickness between the stratosphere and troposphere near this isentropic surface is moderate, which facilitates the study of STE [23,43]. Thus, we selected the 330 K isentropic surface to identify CWB events and investigate their characteristics and role in mass exchange between the stratosphere and troposphere. On the 330 K isentropic surface, the region affected by CWB can be divided into two areas based on PV values. Polygon 1-2-3 represents a high PV region with PV values exceeding 5.5 PVU, while polygon 2-3-4 represents a low PV area with PV values below 5.5 PVU (see Figure 1). These air masses can be transported across various scales to facilitate STE. When the area occupied by high PV air mass, which exhibits stratospheric properties, is larger than the area occupied by low PV air mass, which exhibits tropospheric properties, it is referred to as the equatorward transport type of CWB, favoring STT. Conversely, the poleward transport type of CWB favors TST. In this study, we examine the typical equatorward CWB in the Pacific and the typical poleward CWB in the Atlantic in January 2001 (Figure 1) to investigate the characteristics and differences in stratosphere–troposphere mass transport (TST or STT) induced by different types of CWB.

3.1. Trajectory Analysis in the Equatorward CWB Region

3.1.1. Trajectory of High PV Particles in the CWB Region

Using 00:00 UTC 8 January 2001 as the initial time, we identified 8631 high PV particles and 5259 low PV particles in the equatorward CWB region that occurred in the northeast Pacific Ocean (Figure 1). Backward and forward trajectories were computed for high PV particles and low PV particles separately, covering a 48-h period (Figure 2a,c). These trajectories were then clustered to examine their patterns (Figure 2b,d). In terms of vertical distribution, the atmosphere was divided into three layers: 0–6 km as the lower layer, 6–10 km as the middle layer, and above 10 km as the upper layer.

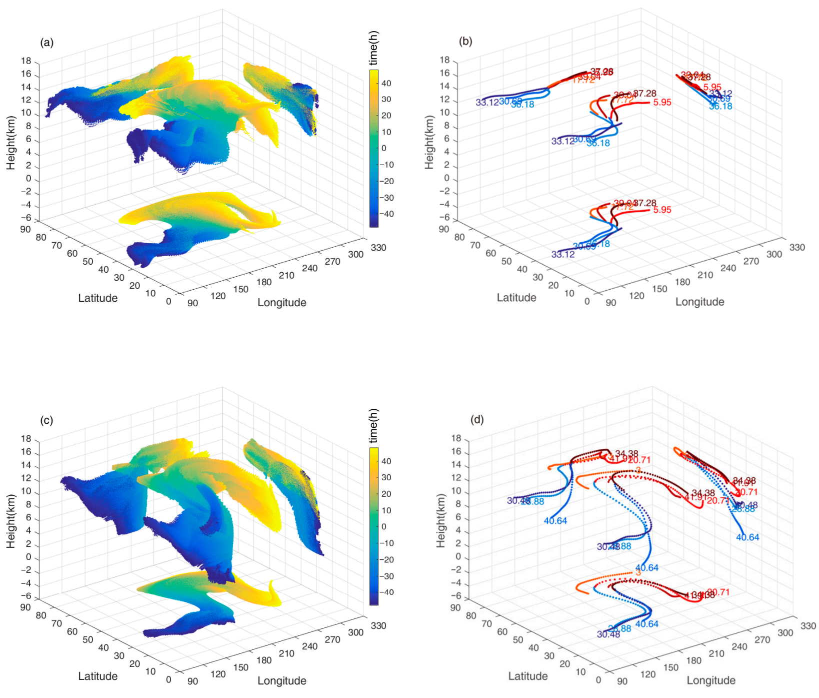

Figure 2. (**a**) The temporal distribution of trajectories for the 8631 high PV particles in the equatorward CWB. The color bar represents the hours relative to the initial moment. (**b**) The distinct red and blue curves represent various forward and backward clustered trajectories from (**a**), respectively. The values in the figure indicate the percentage of particles in each trajectory path relative to the total particles (unit: %). (**c**,**d**) are same as (**a**,**b**), but for the trajectory of 5259 low PV particles.

Analysis of the backward trajectories revealed that high PV particles in the CWB region predominantly followed three paths. Two of these paths were oriented eastward and accounted for 33.12% and 30.69% of the total particles, respectively. Although these paths were similar in direction, they exhibited different velocities. The particles in the southern path moved approximately 90 zonal degrees eastward, while those in the northern path moved approximately 60 degrees eastward (Figure 2b). This discrepancy arose due to the proximity of the black particles to the significant geopotential height gradient contours on the northern side of the high-level westerly jet (Figure 3c,d), resulting in faster movement. Most of the particles in the southern part of the CWB high PV region (Figure 3e) originated from these eastward paths. Additionally, 36.18% of the particles followed a third path characterized by turns (Figure 2b). Starting from 00:00 UTC 7 January, a ridge extended northwestward (Figure 3c–e), and particles on the third path reached the ridge before being transported poleward to approximately 60–70°N. The black particles in the northern part of the CWB high PV region followed this path (Figure 3e). At this stage, the altitudes of these three paths were approximately 11 km, and there was minimal vertical displacement of the particles (Figure 2b). In the vertical profiles, the southern region exhibited positive anomalies in potential height (black contours), while the northern region displayed negative anomalies. The upper-level jet had a maximum zonal wind speed exceeding 50 m·s^{-1} (blue contour) near 30°N from 00:00 UTC 6 January to 00:00 UTC 7 January (Figure 4a–e). Near 40°N, the 330–310 K isentropes were highly compressed, indicating the establishment of the subtropical upper frontal zone. The thermodynamic tropopause (red curve) and the dynamic tropopause (contour lines of 4–6 PVU) were concave, and the average position of the black high PV particles consistently remained above the tropopause at approximately 250 hPa, situated in the extratropical stratosphere.

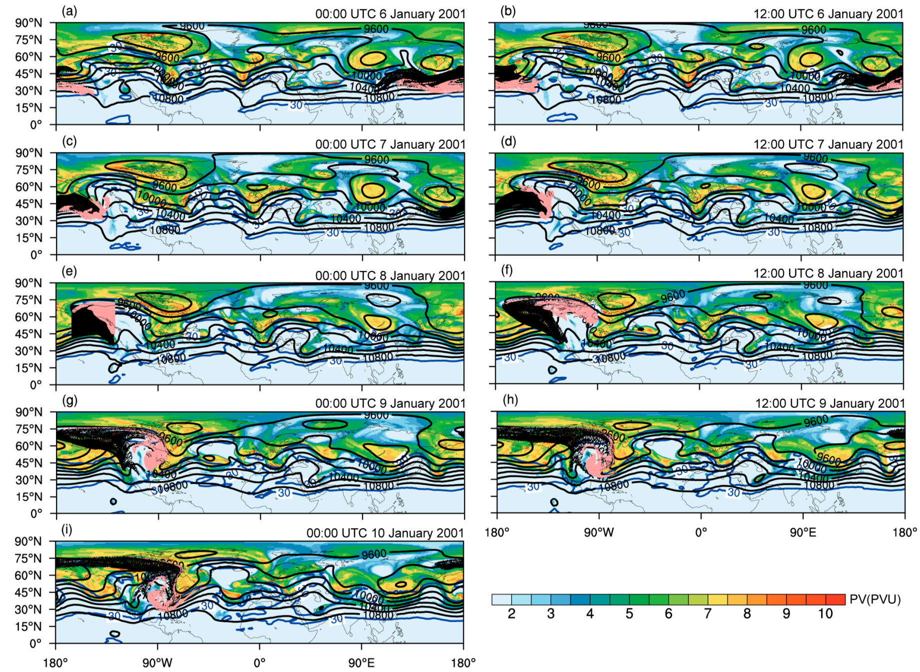

Figure 3. Locations of high PV particles (black dots) and low PV particles (pink dots) at various times (**a**–**i**) on the 250 hPa isobaric surface in the equatorward CWB region. The color bar represents PV values (unit: PVU), and the black contours represent the geopotential height (unit: gpm). The blue contour denotes the zonal wind speed of 30 m·s^{-1}.

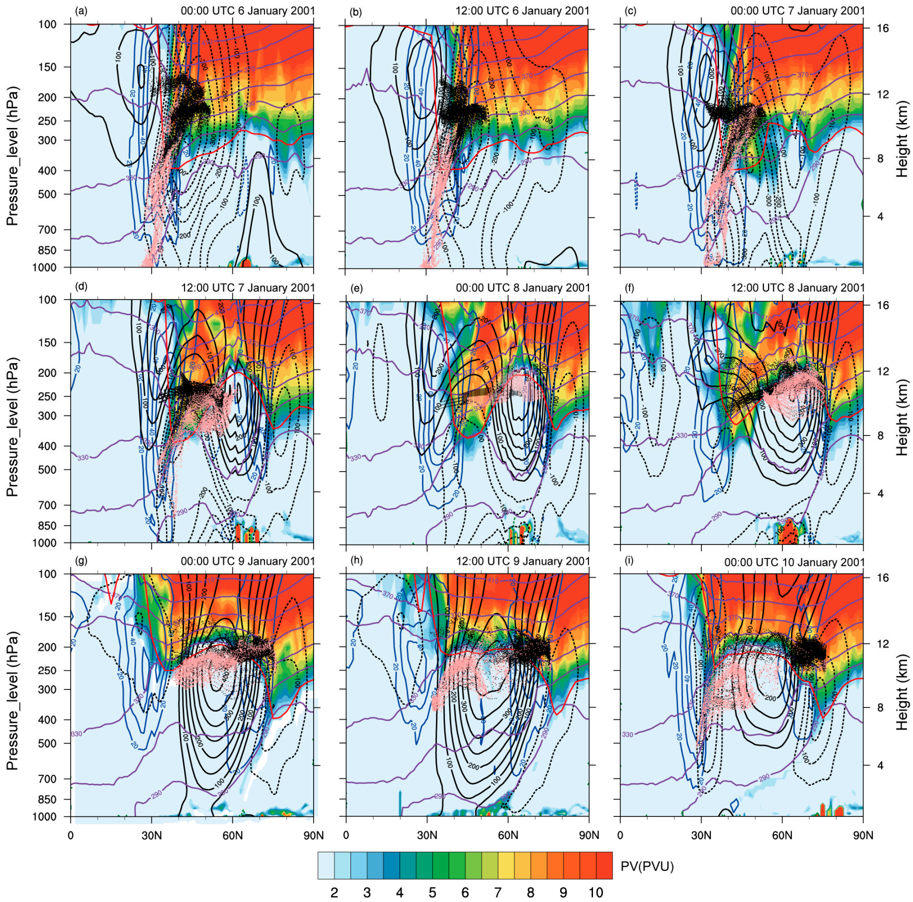

Figure 4. Locations of high PV particles (black dots) and low PV particles (pink dots) at various times (**a**–**i**) in vertical profiles in the equatorward CWB region. The color bar represents PV values (unit: PVU), and the black contours represent the zonal deviation of geopotential height (unit: gpm), with a contour interval of 50 gpm. The blue contours depict the zonal wind, with a contour interval of 10 m·s^{-1}. The purple contours indicate the equipotential temperature lines, with a contour interval of 20 K. The red contours represent the thermodynamic tropopause.

Four distinct forward clustering trajectories were identified for the high PV particles, with three dominant turning paths accounting for 39.04%, 37.28%, and 17.72% of the total particles, respectively (Figure 2b). These particles originated from different meridional positions and followed irregular arcs towards the northeast before turning eastward. The process was primarily influenced by the southwesterly airflow behind the ridge (Figure 3f–i). As the ridge developed northwestward, a positive potential height anomaly was observed in the upper troposphere near 60°N starting from 12:00 UTC 7 January (Figure 4d–i), accompanied by a convex tropopause. The negative potential height anomaly intensified north of the ridge. By 12:00 UTC 9 January (Figure 4h–i), the polar front jet had strengthened (maximum wind speed > 50 m·s^{-1}), and the tropopause exhibited concavity near the upper frontal zone on the northern side of the polar front jet. The high PV particles moved from the upper subtropical frontal zone (around 40–50°N) to the upper polar frontal zone (around 60–70°N). Throughout each trajectory period, vertical movement remained insignificant, and the average pressure (height) of the high PV particles consistently hovered at approximately 250 hPa (near 10 km) (Figures 2b and 4).

3.1.2. Trajectory of Low PV Particles in the CWB Region

There were three backward clustering trajectories observed for low PV particles in the CWB region (Figure 2d), with two of them accounting for 30.48% and 28.88% of the total particles, respectively, representing turning paths. Initially, in the horizontal direction, the particles in these two paths moved eastward from different zonal positions within the latitudes of 30–40°N. Subsequently, they transitioned to poleward and upward transport channels at 150°W. Within 48 h, these particles originated from an altitude of approximately 7 km along the lower edge of the high-level jet and underwent poleward movement of approximately 30 degrees of latitude, ascending to an altitude of approximately 10 km during the second phase. In the early stage, the low PV particles in the two turning paths were advected eastward along the upstream North Pacific jet (pink particles near the large geopotential height gradient contours in Figure 3a,b). As the ridge developed in the exit region of the Pacific jet near 150°W (Figure 3a–e), the southerly flow behind the ridge transported the low PV particles from the jet's exit region to higher latitudes.

The other path was the frontal climbing path, which accounted for 40.64% of the total particles and originated from the lower layers at approximately 2 km. Over a span of 48 h (Figure 2d), these particles were predominantly transported poleward and upward. In the profile sections north of the jet exit zone near 150°N, the 330–310 K isentropic surfaces appeared dense and sagging at approximately 40°N (Figure 4c–e). The ascending motion, induced by the horizontal divergence of the upper-level non-geostrophic airflow, facilitated the poleward and upward transport of low PV particles along the inclined isentropic surface. Eventually, these particles reached approximately 40°N near 250 hPa, remaining within the troposphere due to the convexity of the tropopause (Figure 4e).

There were three distinct southeastward moving paths for low PV particles in the CWB region, accounting for 41.91%, 34.38%, and 20.71% of the total particles, respectively (Figure 2d). On the 250 hPa isobaric surface, the ridge line transitioned from a northwest–southeast to a north–south direction following wave breaking, resulting in the southeastward transport of internal low PV particles along the airflow ahead of the ridge line (Figure 3e–g). Notably, the trajectory of 20.71% of the total particles in Figure 2d exhibited a significant sinking transport during the later period. This sinking was attributed to the particles moving into the airflow behind the trough on the southern side of the downstream (Figure 3g–i). Subsequently, these particles moved southward accompanied by dry cold air, invading into the lower atmospheric levels below 400 hPa (Figure 4h–i).

3.2. Trajectory Analysis in the Poleward CWB Region

3.2.1. Trajectory of High PV Particles in the CWB Region

During the poleward CWB event over the Atlantic (Figure 1b), we identified 2550 high PV particles and 4083 low PV particles within the CWB region using backward and forward trajectory tracking for 48 h each (Figure 5a,c). The trajectories of the high PV and low PV particles were analyzed separately (Figure 5b,d).

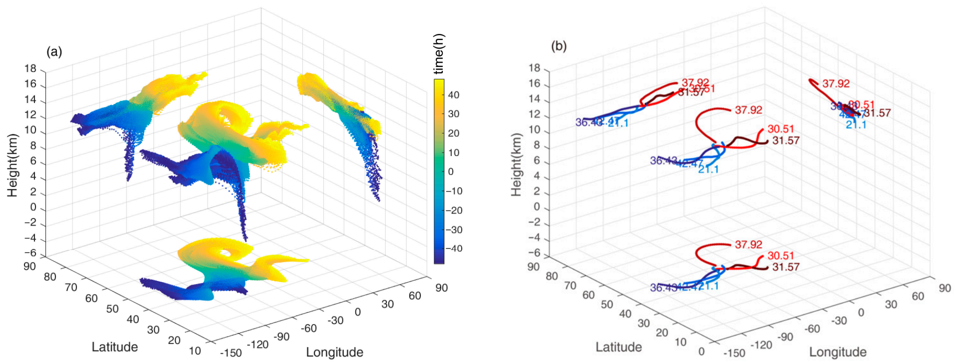

Figure 5. *Cont.*

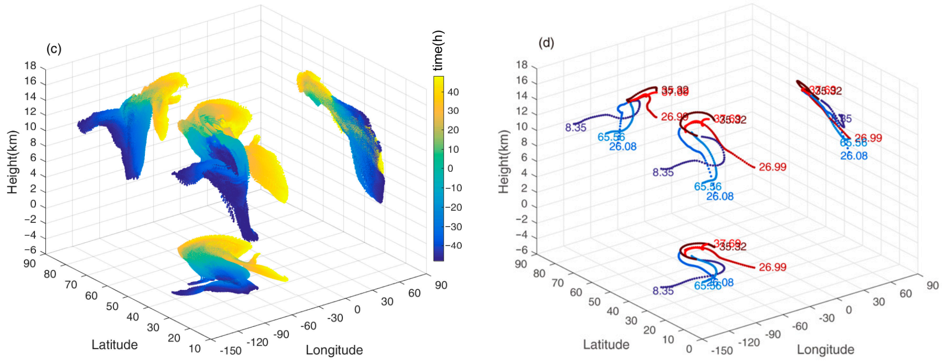

Figure 5. (**a**) The temporal distribution of trajectories for the 2550 high PV particles in the poleward CWB. The color bar represents the hours relative to the initial moment. (**b**) The distinct red and blue curves represent various forward and backward clustered trajectories from (**a**), respectively. The values in the figure indicate the percentage of particles in each trajectory path relative to the total particles (unit: %). (**c**,**d**) are same as (**a**,**b**), but for the trajectory of 4083 low PV particles.

For the high PV particles within the CWB region, three eastward pathways were observed. Although the horizontal speeds differed among these pathways, the vertical displacements remained limited. Within the 48-h period, 36.43% of the particles moved eastward for approximately 60 degrees of longitude, 42.47% moved eastward for nearly 40 degrees of longitude, and 21.10% moved eastward for less than 20 degrees of longitude. These high PV particles primarily originated from the northern edge of the high-level jet over the North America–North Atlantic region (Figure 6a–e). Along the profile sections, the high PV particles remained in the stratosphere near 250 hPa (11 km) over 40°N, following the northern edge of the high-level jet (Figure 7a–e). At this location, the subtropical upper front zone gradually strengthened, and the tropopause exhibited concavity.

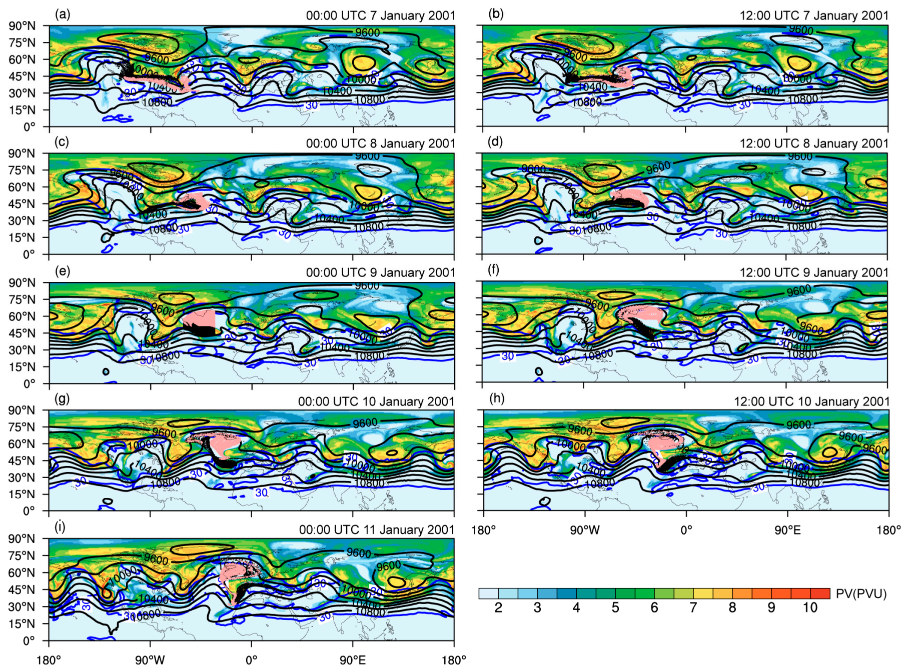

Figure 6. Locations of high PV particles (black dots) and low PV particles (pink dots) at various times (**a**–**i**) on the 250 hPa isobaric surface in the poleward CWB region. The color bar represents PV values (unit: PVU), and the black contours represent the geopotential height (unit: gpm). The blue contour denotes the zonal wind speed of 30 m·s^{-1}.

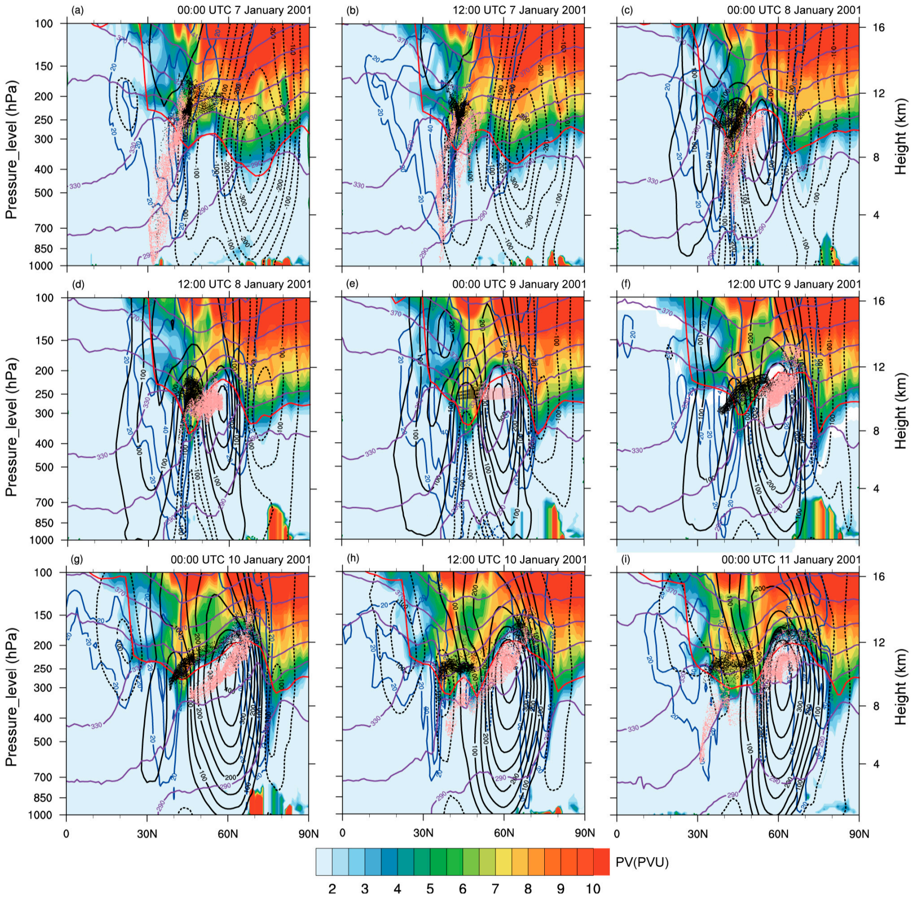

Figure 7. Locations of high PV particles (black dots) and low PV particles (pink dots) at various times (**a**–**i**) in vertical profiles in the poleward CWB region. The color bar represents PV values (unit: PVU), and the black contours represent the zonal deviation of geopotential height (unit: gpm), with a contour interval of 50 gpm. The blue contours depict the zonal wind, with a contour interval of 10 m·s^{-1}. The purple contours indicate the equipotential temperature lines, with a contour interval of 20 K. The red contours represent the thermodynamic tropopause.

In the poleward CWB region, three primary forward trajectories were observed for the high PV particles. A significant proportion, 37.92% of the particles, followed a turning pathway, migrating poleward and upward along the ridge periphery (Figure 6f–h) beyond 60°N, before proceeding southeastward. The updraft of these particles, as depicted in the profile sections (Figure 7h), was linked to the ascent of isentropic surfaces caused by the convexity of the tropopause within the ridge region near 60°N, indicating a positive potential height anomaly. The remaining particles from the other two pathways (31.57% and 30.51%) moved eastward (Figure 5b) and diffused between 30°N and 50°N (Figure 7g–i).

3.2.2. Trajectory of Low PV Particles in the CWB Region

The backward trajectories of low PV particles within the CWB region can be categorized into three distinct pathways. The most prominent pathway, encompassing 65.56% of the total particles, involved an initial eastward transport along the lower edge of the high-level jet, spanning approximately 30 degrees of longitude. Subsequently, these particles turned to migrate poleward and upward within the ridge region (Figures 5d and 6a–e). Another pathway, accounting for 26.08% of the particles, exhibited a poleward and upward motion, covering approximately 25 degrees of latitude meridionally and 4.5 km vertically. The ascending motion on the northern side of the high-level jet's exit region, coupled with the inclined isentropic surfaces of the subtropical upper frontal zone (Figure 7a–e), facilitated upward movement for these particles. Eventually, they entered the upper portion of the ridge beneath the tropopause bulge. A minority of particles followed an alternative pathway.

Within the poleward CWB region, three forward trajectories were observed for the low PV particles. All trajectories exhibited a clockwise motion within the North Atlantic ridge (Figure 5b). The majority of particles were trapped within the northern section of the ridge (Figure 6f–i), while particles in the southernmost part of the ridge (26.99%) were transported southeastward by the northwesterly airflow within the western portion of the southern trough. In the vertical cross-section, these particles descended below the 500 hPa level within the trough region (Figure 7h,i).

3.3. Characteristics of Stratosphere–Troposphere Mass Exchange in the Two Types of CWB Events

Trajectory analysis and profile sections indicate a consistent distribution pattern, with the majority of high PV particles consistently located in the stratosphere, while the majority of low PV particles consistently remained in the troposphere. Only a small fraction of particles underwent STE. However, due to the limited number of particles involved in STE, accurate depiction through trajectory clustering analysis proved challenging. To overcome this limitation, we quantitatively explored the STE process by examining the relative variation in particle proportions based on different PV properties.

In the equatorward CWB region, the initial number of particles was 13,890. Of these, 8086 were located in the stratosphere, 4681 exhibited tropospheric properties, and 1123 resided in the transitional layer. These particles accounted for 58.21%, 33.70%, and 8.08% of the total, respectively. As detailed in Section 2.2.2, a single particle represented an estimated air mass of approximately 3.20×10^{10} kg. Six hours after the onset of CWB, the number of particles in the troposphere and transitional layer started to decrease, while the number of stratospheric particles increased (Figure 8a). Compared with the initial time, an additional 255 particles (1.83% of the total) in the stratosphere suggested a net mass transport of approximately 8.16×10^{12} kg to the stratosphere within six hours of the CWB occurrence. Subsequently, the trend reversed, with a gradual decrease in stratospheric particles and an increase in tropospheric and transitional layer particles. By the 48-h mark following CWB occurrence, the number of stratospheric particles had decreased by 480 (3.45% of the total), while the number of tropospheric particles had increased by 299 (2.15% of the total). Compared with the initial time, approximately 1.54×10^{13} kg of mass was transported from the stratosphere to the troposphere, with approximately 9.57×10^{12} kg crossing the transitional layer to reach the troposphere. The transport from the stratosphere to the troposphere in this equatorward CWB primarily occurred in the later stages, specifically after 36 h following the CWB occurrence.

At the initial moment of the poleward CWB, there were 6633 particles, with 2267 located in the stratosphere, 3814 in the troposphere, and 552 belonging to the transitional layer. These particles accounted for 34.18%, 57.50%, and 8.32% of the total, respectively. The estimated mass of a single particle was approximately 3.71×10^{10} kg. Within the first 6 h after the poleward CWB occurrence, the number of particles in the stratosphere and troposphere exhibited a slow decrease, while the particles in the transition layer began to increase (Figure 8b). However, from 6 to 18 h, the tropospheric particles consistently showed a large negative anomaly, whereas the particles in the stratosphere and transition layer exhibited a positive anomaly. This indicates a significant TST during this period. At the 12th hour after the CWB occurrence, the tropospheric particles reached a maximum decrease of 1.48×10^{13} kg (399 particles, 6.01% of the total), transferring to the transition layer and stratosphere. By the 18th hour, the stratospheric particles increased by 9.39×10^{12} kg (253 particles, 3.81% of the total). Beyond the 18th hour, the stratospheric particles rapidly decreased, while tropospheric particles increased, indicating STT. The transport of particles from the troposphere to the stratosphere in this poleward CWB predominantly occurred in the early stages, specifically within 18 h following the CWB occurrence. Notably, the TST mass in this case was significantly lower compared with a tropopause folding event discussed by Lamarque and Hess [44], where the TST mass was 4.9×10^{14} kg.

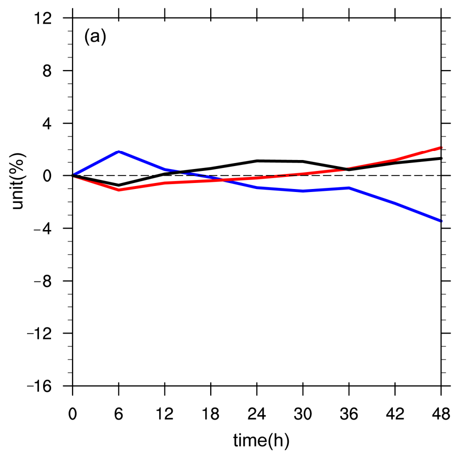

Figure 8. Six-hourly variation of the percentage (unit: %) for each particle attribute in relation to the total particles following the occurrence of equatorward CWB (**a**) and poleward CWB (**b**). The stratospheric attribute particles are represented by the blue solid line, the tropospheric attribute particles by the red solid line, and the transition layer particles by the black solid line.

4. Conclusions and Discussion

Based on the reanalysis data from ERA5, trajectory analysis was conducted on particles in two representative cases of equatorward and poleward cyclonic wave-breaking (CWB) events. Through integration with weather system analysis, the main pathways of particles within the wave-breaking regions and the dominant influencing system were examined. Furthermore, the estimation of stratosphere–troposphere mass exchange characteristics following CWB occurrence in different cases was performed. The key findings are as follows:

The occurrence of CWB events typically coincided with the development of a high-level subtropical front, along with a ridge or a blocking high in the mid-latitudes. Simultaneously, the tropopause exhibited an anomalous pattern characterized by a downward depression in the subtropics and an upward bulge in the mid-latitudes. Consequently, on the boreal extratropical 330 K isentropic surfaces or the 250 hPa isobaric surfaces, a distinct pattern emerged where the southern region was predominantly occupied by stratospheric air, while the northern region was occupied by tropospheric air.

The particles within the wave-breaking region were influenced by the high-level subtropical westerly jet. The majority of high PV particles in the wave-breaking region were transported from the upstream stratosphere along the northern edge of the jet. Following the occurrence of CWB, particle movement was controlled by the ridge or blocking circulation. High PV particles exhibited significant horizontal migration but limited vertical displacement. Conversely, most of the low PV particles in the wave-breaking region were transported from the upstream troposphere along the lower edge of the jet. On average, the low PV particles were located approximately 4 km lower than the high PV particles. Prior to CWB, about one third of the low PV particles moved upward and poleward from the middle–lower troposphere to the tropopause in the middle latitudes, along the inclined isentropic surface within the subtropical high front and ascending motion on the north side of the high-level jet exit region. After CWB, a quarter of the low PV particles moved southward and descended below the 500 hPa isobaric surface, following the northwesterly flow in the downstream trough.

The majority of initial high PV particles in the wave-breaking region were consistently located in the stratosphere, while the low PV particles were predominantly in the troposphere. Only a small fraction (approximately 2% to 6%) of particles underwent STE. In the equatorward CWB case, STE manifested as a net transport from the stratosphere to the troposphere, occurring primarily between 24 to 48 h after the wave-breaking event, with a maximum transported mass of approximately 1.54×10^{13} kg. Conversely, in the poleward CWB case, STE resulted in a net transport from the troposphere to the stratosphere, primarily within 0 to 18 h after CWB occurrence, with a maximum transported mass of approximately 1.48×10^{13} kg.

It is obvious that only one equatorward CWB case and one poleward CWB case have been examined in this study. While efforts were made to consider their representativeness in terms of horizontal scale during case selection, further verification is required to establish their representative role in STE through analysis of additional cases.

Author Contributions: Conceptualization, H.W. and C.S.; data curation, formal analysis, H.W. and C.S.; investigation, resources, validation, visualization, H.W.; writing—original draft, H.W. and C.S.; writing—review and editing, C.S. and D.G. All authors have read and agreed to the published version of the manuscript.

Funding: This work is supported by the National Key Research and Development Plan of China (2022YFF0801703) and the National Natural Science Foundation of China (41875048).

Data Availability Statement: The dataset from ERA5 for this study can be found at https://cds.climate.copernicus.eu/cdsapp#!/search?type=dataset&text=ERA5, accessed on 7 March 2023.

Acknowledgments: We thank ECMWF for the data provision. We acknowledge the high performance computing center of Nanjing University of Information Science and Technology for their support of this work.

Conflicts of Interest: The authors declare no conflict of interest.

References

1. McIntyre, M.E.; Palmer, T.N. Breaking planetary waves in the stratosphere. *Nature* **1983**, *305*, 593–600. [CrossRef]
2. Li, W.; Wang, Z.; Zhang, G.; Peng, M.S.; Benjamin, S.G.; Zhao, M. Subseasonal variability of Rossby wave breaking and impacts on tropical cyclones during the North Atlantic warm season. *J. Clim.* **2018**, *31*, 9679–9695. [CrossRef]
3. Wirth, V.; Riemer, M.; Chang, E.K.M.; Martius, O. Rossby Wave Packets on the Midlatitude Waveguide—A Review. *Mon. Weather Rev.* **2018**, *146*, 1965–2001. [CrossRef]
4. Thorncroft, C.; Hoskins, B.; McIntyre, M. Two paradigms of baroclinic-wave life-cycle behaviour. *Q. J. R. Meteorol. Soc.* **1993**, *119*, 17–55. [CrossRef]
5. Martius, O.; Schwierz, C.; Davies, H.C. Breaking waves at the tropopause in the wintertime Northern Hemisphere: Climatological analyses of the orientation and the theoretical LC1/2 classification. *J. Atmos. Sci.* **2007**, *64*, 2576–2592. [CrossRef]
6. Michel, C.; Rivière, G. The link between Rossby wave breakings and weather regime transitions. *J. Atmos. Sci.* **2011**, *68*, 1730–1748. [CrossRef]
7. Bowley, K.A.; Gyakum, J.R.; Atallah, E.H. A new perspective toward cataloging Northern Hemisphere Rossby wave breaking on the dynamic tropopause. *Mon. Weather Rev.* **2019**, *147*, 409–431. [CrossRef]
8. Papin, P.P.; Bosart, L.F.; Torn, R.D. A feature-based approach to classifying summertime potential vorticity streamers linked to Rossby wave breaking in the North Atlantic basin. *J. Clim.* **2020**, *33*, 5953–5969. [CrossRef]
9. Appenzeller, C.; Davies, H.C. Structrue of stratopsheric intrusions into the troposphere. *Nature* **1992**, *358*, 570–572. [CrossRef]
10. Norton, W.A. Breaking Rossby waves in a model stratosphere diagnosed by a vortex-following coordinate system and a technique for advecting material contours. *J. Atmos. Sci.* **1994**, *51*, 654–673. [CrossRef]
11. Holton, J.R.; Haynes, P.H.; McIntyre, M.E.; Douglass, A.R.; Rood, R.B.; Pfister, L. Stratosphere-troposphere exchange. *Rev. Geophys.* **1995**, *33*, 403–440. [CrossRef]
12. Postel, G.A.; Hitchman, M.H. A climatology of Rossby wave breaking along the subtropical tropopause. *J. Atmos. Sci.* **1999**, *56*, 359–373. [CrossRef]
13. Schoeberl, M.R.; Ueyama, R.; Pfister, L. A Lagrangian view of seasonal stratosphere-troposphere exchange. *J. Geophys. Res. Atmos.* **2022**, *127*, e2022JD036772. [CrossRef]
14. Wang, H.; Wang, W.; Shangguan, M.; Wang, T.; Hong, J.; Zhao, S.; Zhu, J. The Stratosphere-to-Troposphere Transport Related to Rossby Wave Breaking and Its Impact on Summertime Ground-Level Ozone in Eastern China. *Remote Sens.* **2023**, *15*, 2647. [CrossRef]
15. Zhu, J.; Jin, X.; Shi, C.; Chen, D. The Troposphere-to-Stratosphere Transport Caused by a Rossby Wave Breaking Event over the Tibetan Plateau in Mid-March 2006. *Remote Sens.* **2023**, *15*, 155. [CrossRef]
16. Langford, A.O.; Pierce, R.B.; Schultz, P.J. Stratospheric intrusions, the Santa Ana winds, and wildland fires in Southern California. *Geophys. Res. Lett.* **2015**, *42*, 6091–6097. [CrossRef]
17. Sullivan, J.T.; McGee, T.J.; Thompson, A.M.; Pierce, R.B.; Sumnicht, G.K.; Twigg, L.W.; Eloranta, E.; Hoff, R.M. Characterizing the lifetime and occurrence of stratospheric-tropospheric exchange events in the rocky mountain region using high-resolution ozone measurements. *J. Geophys. Res. Atmos.* **2015**, *120*, 12410–12424. [CrossRef]

18. Yang, H.; Chen, G.; Tang, Q.; Hess, P. Quantifying isentropic stratosphere-troposphere exchange of ozone. *J. Geophys. Res. Atmos.* **2016**, *121*, 3372–3387. [CrossRef]
19. Zhang, J.; Tian, W.; Xie, F.; Chipperfield, M.P.; Feng, W.; Son, S.W. Stratospheric ozone loss over the Eurasian continent induced by the polar vortex shift. *Nat. Comm.* **2018**, *9*, 206. [CrossRef]
20. Xie, F.; Tian, W.; Zhou, X.; Zhang, J.; Xia, Y.; Lu, J. Increase in lower stratospheric water vapor in the past 100 years related to tropical Atlantic warming. *Geophys. Res. Lett.* **2021**, *47*, e2020GL090539. [CrossRef]
21. Zhou, X.; Chen, Q.; Li, Y.; Zhao, Y.; Lin, Y.; Jiang, Y. Impacts of the Indo-Pacific warm pool on lower stratospheric watervapor: Seasonality and hemispheric contrasts. *J. Geophys. Res. Atmos.* **2021**, *126*, e2020JD034363. [CrossRef]
22. Qie, K.; Wang, W.; Tian, W.; Huang, R.; Xu, M.; Wang, T.; Peng, Y. Enhanced upward motion through the troposphere over the tropical western Pacific and its implications for the transport of trace gases from the troposphere to the stratosphere. *Atmos. Chem. Phys.* **2022**, *22*, 4393–4411. [CrossRef]
23. Homeyer, C.R.; Bowman, K.P. Rossby wave breaking and transport between the tropics and extratropics above the subtropical jet. *J. Atmos. Sci.* **2013**, *70*, 607–626. [CrossRef]
24. Manney, G.L.; Hegglin, M.I.; Daffer, W.H.; Schwartz, M.; Santee, M.; Pawson, S. Climatology of Upper Tropospheric–Lower Stratospheric (UTLS) Jets and Tropopauses in MERRA. *J. Clim.* **2014**, *27*, 3248–3271. [CrossRef]
25. Jing, P.; Banerjee, S. Rossby wave breaking and isentropic stratosphere-troposphere exchange during 1981–2015 in the Northern Hemisphere. *J. Geophys. Res. Atmos.* **2018**, *123*, 9011–9025. [CrossRef]
26. Draxler, R.R.; Hess, G.D. An overview of the HYSPLIT_4 modeling system of trajectories, dispersion, and deposition. *Aust. Meteorol. Mag.* **1998**, *47*, 295–308.
27. Mcgowan, H.; Clark, A. Identification of dust transport pathways from Lake Eyre, Australia using Hysplit. *Atmos. Environ.* **2008**, *42*, 6915–6925. [CrossRef]
28. Tanvir, A.; Javed, Z.; Jian, Z.; Zhang, S.; Bilal, M.; Xue, R.; Wang, S.; Bin, Z. Ground-Based MAX-DOAS Observations of Tropospheric NO_2 and HCHO During COVID-19 Lockdown and Spring Festival Over Shanghai, China. *Remote Sens.* **2021**, *13*, 488. [CrossRef]
29. Attiya, A.A.; Jones, B.G. Impact of smoke plumes transport on air quality in Sydney during extensive bushfires (2019) in New South Wales, Australia using remote sensing and ground data. *Remote Sens.* **2022**, *14*, 5552. [CrossRef]
30. Bao, C.; Yong, M.; Bueh, C.; Bao, Y.; Jin, E.; Bao, Y.; Purevjav, G. Analyses of the Dust Storm Sources, Affected Areas, and Moving Paths in Mongolia and China in Early Spring. *Remote Sens.* **2022**, *14*, 3661. [CrossRef]
31. Choi, D.S.; Choi, S.M.; Choi, H. Abrupt high PM concentration in an urban calm cavity generated by internal gravity waves and a shallow coastal atmospheric boundary layer with the influence of the yellow dust from China. *Remote Sens.* **2023**, *15*, 372. [CrossRef]
32. Brimelow, J.C.; Reuter, G.W. Transport of Atmospheric Moisture during Three Extreme Rainfall Events over the Mackenzie River Basin. *J. Hydrometeorol.* **2005**, *6*, 423–440. [CrossRef]
33. Jiang, Z.; Jiang, S.; Shi, Y.; Liu, Z.; Li, W.; Li, L. Impact of moisture source variation on decadal-scale changes of precipitation in North China from 1951 to 2010. *J. Geophys. Res. Atmos.* **2017**, *122*, 600–613. [CrossRef]
34. Hao, C.; Song, L.; Zhao, W. HYSPLIT-based demarcation of regions affected by water vapors from the South China Sea and the Bay of Bengal. *Eur. J. Remote Sens.* **2021**, *54*, 348–355. [CrossRef]
35. Hwang, S.H.; Kim, J.; Cho, G.R. Observation of secondary ozone peaks near the tropopause over the Korean peninsula associated with stratosphere-troposphere exchange. *J. Geophys. Res.* **2007**, *112*, D16305. [CrossRef]
36. Song, Y.; Lü, D.; Li, Q.; Bian, J.; Wu, X.; Li, D. The impact of cut-off lows on ozone in the upper troposphere and lower stratosphere over Changchun from ozonesonde observations. *Adv. Atmos. Sci.* **2016**, *33*, 135–150. [CrossRef]
37. Wang, Y.Q.; Zhang, X.Y.; Draxler, R.R. Traj Stat: GIS-based software that uses various trajectory statistical analysis methods to identify potential sources from longterm air pollution measurement data. *Environ. Modell. Softw.* **2009**, *24*, 938–939. [CrossRef]
38. Sirois, A.; Bottenheim, J.W. Use of backward trajectories to interpret the 5-year record of PAN and O_3 ambient air concentrations at Kejimkujik National Park, Nova Scotia. *J. Geophys. Res. Atmos.* **1995**, *100*, 2867–2881. [CrossRef]
39. Hoerling, M.P.; Schaack, T.K.; Lenzen, A.J. Global objective tropopause analysis. *Mon. Weather Rev.* **1991**, *119*, 1816–1831. [CrossRef]
40. Hoinka, K.P. Mean global surface pressure series evaluated from ECMWF reanalysis data. *Q. J. R. Meteor. Soc.* **1998**, *124*, 2291–2297. [CrossRef]
41. Randel, W.J.; Seidel, D.J.; Pan, L.L. Observational characteristics of double tropopauses. *J. Geophys. Res. Atmos.* **2007**, *112*, D07309. [CrossRef]
42. Kunz, T.; Fraedrich, K.; Lunkeit, F. Impact of synopticscale wave breaking on the NAO and its connection with the stratosphere in ERA-40. *J. Clim.* **2009**, *22*, 5464–5480. [CrossRef]
43. Kunz, A.; Konopka, P.; Müller, R.; Pan, L. Dynamical tropopause based on isentropic potential vorticity gradients. *J. Geophys. Res. Atmos.* **2011**, *116*, D01110. [CrossRef]
44. Lamarque, J.F.; Hess, P.G. Cross-tropopause mass exchange and potential vorticity budget in a simulated tropopause folding. *J. Atmos. Sci.* **1994**, *51*, 2246–2269. [CrossRef]

Disclaimer/Publisher's Note: The statements, opinions and data contained in all publications are solely those of the individual author(s) and contributor(s) and not of MDPI and/or the editor(s). MDPI and/or the editor(s) disclaim responsibility for any injury to people or property resulting from any ideas, methods, instructions or products referred to in the content.